ROLE OF THE STABILIZING SHELL IN HIGH-β, LOW-q DISRUPTIONS IN PBX-M

M. OKABAYASHI, N. POMPHREY, J. MANICKAM,
D.J. WARD[a], R.E. BELL, R.E. HATCHER, R. KAITA,
S.M. KAYE, H.W. KUGEL, B. LeBLANC,
F.M. LEVINTON[b], D.W. ROBERTS[c],
S. SESNIC, Y. SUN, H. TAKAHASHI
Princeton Plasma Physics Laboratory, Princeton University,
Princeton, New Jersey,
United States of America

ABSTRACT. The characteristics of high-β, low-q disruptions have been studied in PBX-M, a device with a nearby conducting shell. The coupling between the wall and the plasma was varied by choosing different plasma shapes, including nearly circular plasmas, D-shaped plasmas and bean-shaped plasmas (indented on the midplane), and by increasing the effective coverage of the plasma by the shell. Disruption precursors were observed to have a strong dependence on the coupling between the plasma and the shell. Measured mode growth times vary from between several times the Alfvén time-scale (~ 100 μs) to the L/R time-scale of the wall (~ 20 ms). The behaviour of observed disruption precursors is interpreted in terms of the resistive wall mode theory of ideal plasmas, and a detailed calculation of the stability of a strongly coupled bean configuration using the NOVA-W linear stability code is presented. The experimental observations are in good agreement with the theoretical predictions.

1. INTRODUCTION

Reactor and next generation tokamak design studies, such as ARIES, SSTR, ITER and TPX [1–5], have identified attractive high-β operating scenarios (e.g., reverse shear [6–8]) that can lead to economically attractive steady state reactors. Such high-β scenarios will only be relevant to steady state reactors if they can be demonstrated to be free of major disruptions.

Experimental results from large tokamak experiments, such as TFTR, DIII-D and PBX, have reported that the excitation of low-n external kink and kink ballooning instabilities are responsible for the disruptions that occur at low q and high β [9–12]. Stability issues of the external kink mode have been identified as one of the highest priorities in the R&D programmes for TPX and ITER.

An effective method of stabilizing the external kink mode involves the use of a nearby conducting shell, also referred to as a wall, surrounding the plasma. (In this paper we shall use the terms wall and shell interchangeably to refer to the external conducting structure used to stabilize the kink mode.) If the shell is perfectly conducting and placed sufficiently close to the plasma edge, external kinks can be completely stabilized. In practice, however, the shell has finite resistivity, and ideal MHD theory shows that the growth time of the external kink mode can only be slowed from the ideal time-scale, $\tau_{Alf} \sim$ tens of microseconds, to the time-scale of the resistive shell, $\tau_{L/R} \sim$ tens to hundreds of milliseconds. To be relevant for steady state reactors, stabilization must be demonstrated for much longer times.

Recent numerical results [13–16] and analytic theory [17–19] have shown that low-n ideal pressure or current driven external kink modes can be completely stabilized by plasma toroidal rotation, in combination with a resistive wall and plasma viscous dissipation (parallel or perpendicular). These results suggest the possibility of obtaining significant increases in experimental β limits,

[a] Centre de recherche en physique des plasmas, Association Euratom-Confédération Suisse, Ecole polytechnique Fédérale Lausanne, Switzerland.
[b] Fusion Physics and Technology, Torrance, California, United States of America.
[c] Lawrence Livermore National Laboratory, Livermore, California, United States of America.

TABLE I. COMPARISON OF PLASMA PERFORMANCE WITH AND WITHOUT A CONDUCTING SHELL

(R is the plasma major radius, a is the midplane minor radius, ϵ is the inverse aspect ratio, β is the volume averaged plasma beta, β_c^∞ is the β limit for n = 1 modes calculated by the PEST stability code with a conducting wall at infinity, q_{95} is the safety factor at the 95% flux surface, I_p is the plasma current and B_t is the toroidal magnetic field)

	PBX (without shell)	PBX-M (with shell)
R (m)	1.45	1.65
a (m)	0.3	0.3
$\epsilon^{-1} = R/a$	4.3	5.5
β (%)	5.5	6.8
β_c^∞ (%)	3.5	3.0
β/ϵ (%)	27	38
β/β_c	1.6	2.3
q_{95}	3.3	3.1
I_p (kA)	550	580
B_t (T)	0.9	1.1
Indentation (%)	22	27

without the need for external intervention by an active feedback system. Stability requires that the plasma rotation be sufficiently rapid (typically at least 10 to 40% of the ion sound speed), and that the resistive wall be located at a radius r_w that lies within a range $r_\Omega < r_w < r_c$, bounded from above by the critical radius, r_c, at which a perfectly conducting wall would stabilize the kink, and bounded from below by some other radius, r_Ω, whose value depends on the plasma rotation frequency, Ω. A detailed discussion of the requirements for the stability of resistive wall modes will be presented later, in Section 2.

Explorations of resistive wall mode issues have begun at DIII-D and PBX-M. DIII-D [16, 20, 21] has a thin, poloidally continuous, Inconel vacuum vessel, with $\tau_{L/R} \approx$ 1–2 ms. Sustained values of β were achieved that are approximately 30% higher than the predicted β limit from ideal MHD stability calculations that assume no conducting wall. Furthermore, a clear correlation was observed between loss of toroidal rotation at the $q = 2$ plasma surface and gain of MHD activity: disruptions due to external kinks occur when the observed mode rotation frequency falls below 1 kHz [16, 21, 22].

The effect of a conducting shell on plasma performance has also been studied in PBX-M [23]. In this paper, we provide a detailed description of PBX-M disruption precursors with an interpretation based on the present understanding of resistive wall mode theory.

The conducting shell in PBX-M is a poloidally segmented aluminium shell with a time constant of $\tau_{L/R} \approx$ 40 ms, which covers over 70% of the plasma surface [24]. A comparison of plasma performance in PBX-M [23] with that in PBX [25, 26] (which had a similar plasma configuration but no conducting shell) is given in Table I. Since the aspect ratio of the plasma was increased to accommodate the stabilizing shell in PBX-M, one must take into account the aspect ratio scaling of β at constant q, namely $\beta \propto \epsilon$, when comparing the performance of the two devices. It is found that β/ϵ for PBX-M is increased by a factor of 1.4 compared with the equivalent value for PBX.

Magnetic perturbations due to plasma instability generate eddy currents in the surrounding conducting shell. In PBX-M, all high-β disruptions have precursors that are observable in the eddy current pattern. The eddy current observations are an extremely useful diagnostic

for disruptions and for the study of resistive wall modes. In this paper, we summarize the characteristics of high-β disruption precursors for various plasma configurations, relating the observations to the present theory of resistive wall external kink modes for ideal plasmas.

A review of resistive wall mode theory is given in Section 2, to provide a framework for discussion of the PBX-M disruption results. Section 3 describes the PBX-M conducting shell. Section 4 describes the plasma configurations used for the present study. Various plasma shapes are considered (circular, D shapes and bean shapes), which correspond to a range of plasma–shell coupling strengths. Typical disruption precursors are described, with particular emphasis on eddy current measurements at the conducting shell. Circular plasmas are weakly coupled to the conducting shell, show rapid mode rotation (comparable to the plasma toroidal rotation velocity), fast growth rates (on the ideal MHD (Alfvén) time-scale) and little influence of the conducting shell on the MHD behaviour. Bean shaped plasmas, on the other hand, are strongly coupled to the conducting shell. Growth rates are comparable to the L/R time-scale of the conducting shell, and observed frequencies are nearly zero compared with the plasma rotation frequency. This is an important characteristic of resistive wall modes. D-shaped plasmas show disruption precursor behaviour that is intermediate between those of circular and bean shaped plasmas. In Section 5, a detailed calculation using the NOVA-W stability code is presented of the effect of toroidal plasma rotation on the resistive wall mode stability of a strongly coupled bean configuration. Good agreement is found between the code predictions of growth rate and mode frequency and the experimental data. The requirement on plasma rotation velocity for producing complete stability of the resistive wall modes is explored. Finally, a summary and conclusions are presented in Section 6.

2. OVERVIEW OF RESISTIVE WALL MODE THEORY

Following the initial numerical results of Bondeson and Ward [13], who demonstrated the possibility of complete stabilization of external kink modes by plasma toroidal rotation in combination with a resistive wall and plasma sound wave damping, a theory of resistive wall modes for ideal plasmas has emerged [14–19]. In this section, we describe the salient features of the theory in order to provide a framework for the discussion of PBX-M disruptions.

Numerical and analytic studies show that external kink-unstable rotating plasmas surrounded by a conducting wall have two modes of physical interest; the 'plasma mode' and the 'resistive wall mode'. In the limit of zero wall conductivity, the plasma mode is identical to the usual ideal external kink mode; the resistive wall mode is introduced when the wall conductivity is made finite. For fixed plasma conditions (i.e. pressure and current profiles, and toroidal rotation frequency, Ω) the plasma mode and the resistive wall mode behave in opposite ways with respect to variation of the distance separating the plasma and the wall. Let us normalize all distances by the midplane plasma radius, and let $\hat{r}_w$ denote the normalized radial distance of the wall from the centre of the plasma. The plasma mode is stable whenever the wall is *closer* to the plasma than the critical radius, $\hat{r}_c$, at which a perfectly conducting wall stabilizes the plasma; the value of $\hat{r}_c$ is independent of Ω but depends on the plasma current and pressure profiles. The resistive wall mode, however, is stable when the wall is *further* from the plasma than some (other) critical radius, $\hat{r}_\Omega$, whose value depends on the rotation frequency, and decreases when the rotation frequency is increased. For sufficiently rapid plasma rotation (typically 10 to 40% of the ion sound speed), there is a stable window of plasma–wall separation (see Fig. 1(a)), which becomes wider as the rotation speed is increased. For fixed current and pressure profiles, robust stability with respect to changes in the plasma rotation frequency is provided by resistive walls with $\hat{r}_w$ as close as possible to $\hat{r}_c$.

The resistive wall mode penetrates the resistive wall and rotates with respect to the wall with a frequency that is much smaller than the plasma rotation frequency ($\omega/\Omega \ll 1$). The plasma mode, on the other hand, can rotate with $\omega \approx \Omega$. If the mode frequency is sufficiently high (typically 10 times the inverse L/R time of the wall) [14, 15, 18], the rotating eddy current has insufficient time to leak through the wall; the wall acts like a perfect conductor and stability is achieved.

The existence of plasma dissipation is crucial for the development of a stability window. For pressure driven kink modes, toroidal coupling to sound waves, which are affected by ion Landau damping, has been identified as an effective dissipation mechanism [13]. Fluid approximations to sound wave damping are used in numerical calculations, such as the NOVA-W calculation [14] reported later in this paper, and parallel fluid viscosity provides the damping. For current driven kink modes, anomalous perpendicular viscosity provides an effective damping mechanism [15, 18].

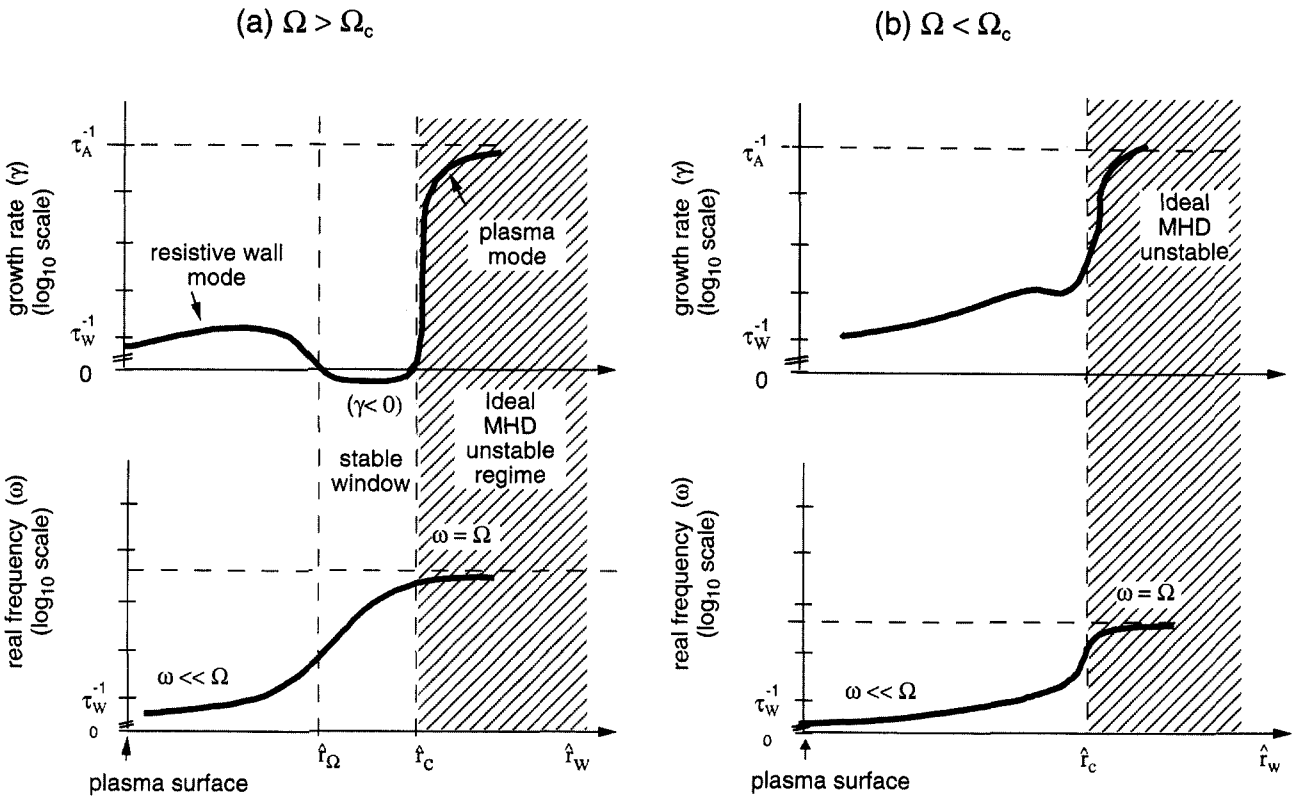

FIG. 1. Schematic diagram of resistive wall mode theory predictions of the dependence of the external kink growth rate (γ) and mode frequency (ω) on resistive wall location, $\hat{r}_w = r_w/a$, normalized by the plasma midplane radius. (a) The plasma rotation frequency, Ω, is sufficiently large ($>\Omega_c$) to stabilize the external kink mode for resistive wall positions in the range $\hat{r}_\Omega < \hat{r}_w < \hat{r}_c$. (b) The plasma rotation frequency is insufficient to open a stability window ($\Omega < \Omega_c$). $\hat{r}_c$ is the (normalized) critical radius at which an ideal conducting wall completely stabilizes the external kink. τ_w and τ_A are the resistive wall and Alfvén (MHD) time-scale, respectively. The vertical scale in the plots is logarithmic, with a factor of 10 separating each mark. The relative values of τ_A^{-1}, τ_w^{-1} and Ω are 'typical' for present day tokamak experiments.

The simplified discussion given above assumes rigid plasma rotation, with Ω = constant. In reality, the plasma rotation is not rigid, and Ω has a spatially varying profile. Typical toroidal rotation velocities in PBX-M, for example, are 200 km/s at the centre of the plasma and 10 km/s near the edge (see Fig. 8(b), Section 4.4), so what value of Ω is relevant? Since sound wave damping is a resonance phenomenon active near rational q surfaces, and since damping is greatest in regions of large pressure, one would expect that it is Ω at the integer q surface closest to the magnetic axis that is important for resistive wall mode stability. Experimental data from DIII-D plasmas with $q(0) > 1$ confirm a strong correlation between maintaining plasma rotation at the $q = 2$ surface and maintaining plasma stability with respect to external kink modes [16, 20, 21]. Numerical simulation [14] also indicates enhanced kink stability as additional rational q surfaces appear in the plasma.

Figure 1(a) was drawn assuming conditions sufficient to produce a window of complete stability. Figure 1(b) shows a sketch of the mode growth rate and mode frequency when Ω is close to, but slightly less than, the critical value required to open the stability window. The growth rate of the plasma mode makes a smooth transition, over a narrow range of $\hat{r}_w$ values, from the ideal MHD (Alfvén) time-scale to the time-scale of the resistive wall, but the mode does not completely stabilize. In this narrow region of wall positions, the plasma mode changes from rotating with the plasma ($\omega \approx \Omega$) to being essentially locked to the wall ($\omega < \tau_w^{-1} \ll \Omega$).

The resistive (i.e. actual) wall position, $\hat{r}_w$, relative to the critical ideal wall position, $\hat{r}_c$, is an important determinant of external kink mode behaviour: if $\hat{r}_w > \hat{r}_c$, the plasma is ideally unstable and the influence of the resistive wall on the growth rate and mode frequency is weak. In this case, we will describe the plasma–shell coupling as 'weak'. If, on the other hand, $\hat{r}_w < \hat{r}_c$, the resistive shell can have a strong influence on the plasma behaviour: the mode growth rate can be slowed to the inverse L/R time-scale of the conducting shell, and the mode can essentially lock to the wall. In this case the plasma–shell coupling will be described as 'strong'. The transition region, where $\hat{r}_w \lessapprox \hat{r}_c$, is a region where the resistive wall mode frequency and growth rate can vary considerably. Since, for a fixed wall position, a change in plasma profile causes a change in $\hat{r}_c$ relative to $\hat{r}_w$, one expects to find a sensitive dependence of mode frequency and growth rate on profile fluctuations.

The PBX-M disruption data presented in Section 4 correspond to a variety of plasma configurations (circular, D and bean) which are chosen to have different plasma–shell coupling strengths, with different relative values of $\hat{r}_w$ and $\hat{r}_c$. The data will be interpreted, whenever possible, in terms of the resistive wall mode theory reviewed above.

3. PBX-M CONDUCTING SHELL

PBX-M is a medium size large aspect ratio tokamak, with major radius $R = 1.65$ m, midplane minor radius $a = 0.30$ m (aspect ratio $A = R/a = 5.5$), and elongation $\kappa = 1.2$–2.1. A flexible poloidal field coil system allows production of a wide variety of plasma shapes, from nearly circular configurations to strongly indented bean configurations. Plasma heating is mainly by neutral

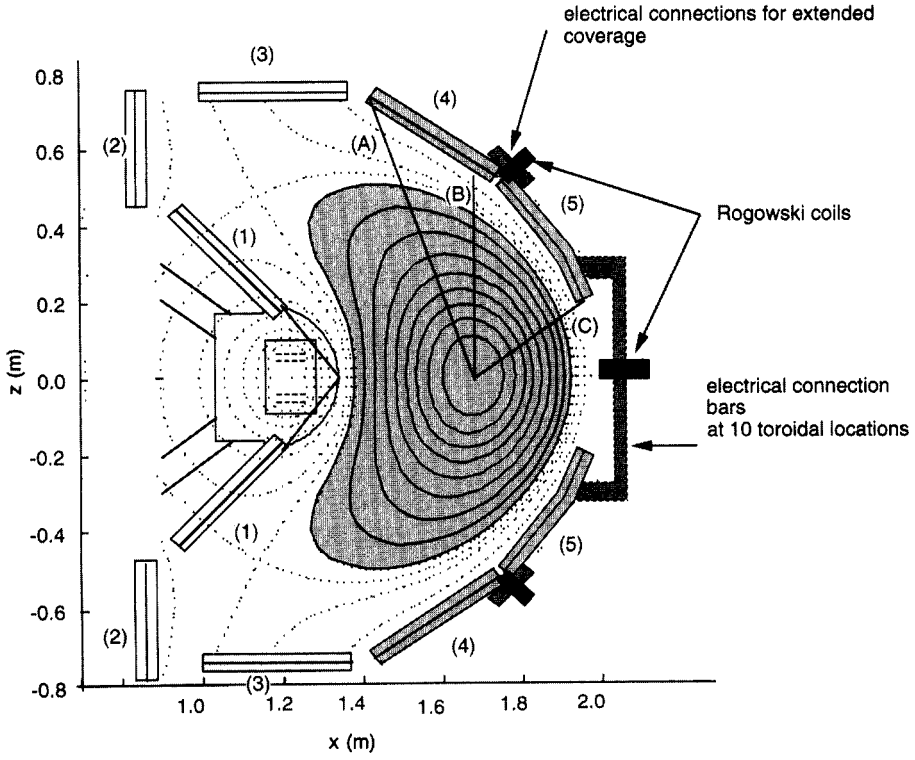

FIG. 2. The PBX-M conducting plate arrangement. Ten poloidally segmented aluminium plates are located symmetrically with respect to the z = 0 *plane. The plates Nos 1, 2 and 3 function primarily as the* n = 0 *passive stabilization system. Plates Nos 4 and 5 are the* n = 1 *external kink stabilizers and have an* L/R *time constant of* τ_w = 30–40 *ms. The rays labelled (A), (B) and (C) are radius vectors from the plasma geometric centre to the* n = 1 *conducting plates, along which plasma–shell separation distances are tabulated in Table II.*

beam injection (NBI), with two parallel (3 MW) and two perpendicular (4 MW) NBI sources and a pulse length of 300 ms. The plasma duration is 0.5 to 1.0 s. Typical central toroidal flow velocities are 250 km/s. As shown in Fig. 2, a close-fitting conducting shell surrounds the plasma. The outboard sections of the shell were installed as part of an upgrade of the original PBX experiment [26], with the intention of improving MHD stability near the beta limit. The results already shown in Table I attest to the ability of the shell to enhance the achievable β.

The PBX-M conducting shell (see Fig. 2) is segmented poloidally into 10 plate sections located symmetrically with respect to the $z = 0$ plane. Each stabilizing plate is made of 2.5 cm thick aluminium and has a single toroidal electrical gap to prevent one turn toroidal current paths. The outer plates (Nos 5 and/or 4) serve as a passive stabilization system for $n = 1, 2$ and 3 modes: the top and bottom members of the plates (Nos 5) are connected at 10 toroidal locations with electrical junction bars on the midplane, allowing the generation of helical eddy current flows. In addition, plates Nos 4 and 5 can be connected by 10 junction bars, leading to a configuration with 'extended shell coverage'. The top and bottom members of the inner shell plates Nos 1, 2 and 3 are saddle connected, and function as an $n = 0$ stabilizing system. The passive plates Nos 5 with the 10 midplane electrical jumpers also serve as a stabilizer for $n = 0$ vertical motion by allowing a distributed saddle current [27].

To determine the eddy current characteristics in the complex 3-D shell structure, and to calculate their decay time constants, detailed simulations have been performed with the 3-D SPARK electromagnetics code [28] using $m/n = 3/1$ and $m/n = 2/1$ helical current filaments. The eddy current through the midplane jumpers, $I_{eddy}(\phi_j, t)$, where ϕ_j, $j = 1, 2, \ldots, 10$, is the toroidal angle of the jumpers, is decomposed into toroidal eigenmodes with $n = 1, 2, 3$. For an $m/n = 3/1$ helical filament located at $r/a = 0.7$, the $n = 1$ eigenmode decay constant is between 30 and 40 ms, and for an $m/n = 2/1$ filament the time constant is between 20 and 40 ms [27].

Rogowski coils are located on each junction bar and determine the shell eddy current distribution during the experiments. The real time acquisition of global eddy current patterns is an excellent diagnostic for global low-n kink instabilities, as it is relatively simple to extract specific low-n information from the toroidally distributed Rogowski coils. In contrast, Mirnov coil data measure local magnetic fields and require post-shot analysis to elicit the same global information.

4. DISRUPTION PRECURSORS IN HIGH-β, LOW-q DISCHARGES

4.1. Plasma configurations

In the following subsections, we describe the characteristic MHD behaviour of PBX-M plasmas during high-β, low-q operation, focusing on the role played by the conducting wall in determining the observed behaviour. In view of the theory of resistive wall modes outlined in Section 2, various plasma shapes are considered that represent varying strengths of plasma–shell coupling:

(a) Circular plasmas with plates Nos 4 and 5 electrically connected. The plasma–shell separation is substantial, therefore the plasma–shell coupling is weak.
(b) D-shaped plasmas with plates Nos 4 and 5 electrically connected. These plasmas are also weakly coupled to the shell.
(c) Bean-shaped plasmas with and without electrical connection between plates Nos 4 and 5. These plasmas are in close proximity to the conducting plates and are therefore strongly coupled to the shell.

Equilibrium flux plots for circular, D-shaped and bean-shaped plasma configurations are shown in Fig. 3. Clearly, for a given plasma shape, the separation distance between the plasma and the shell is not uniform around the plasma surface. Table II quantifies the variation in plasma–shell separation. In the first three columns of the table, the ratio of the distance from the plasma centre to the shell to the plasma radius is tabulated. Distances are measured along the directions labelled A, B and C in Fig. 2, namely:

(A) From the plasma geometric centre (at $R = 1.65$ m) to the corner of minimum major radius of plate No. 4,
(B) Along a vertical chord from the plasma centre to plate No. 4,
(C) From the plasma centre to the point of maximum major radius of plate No. 5.

To relate the observed MHD behaviour to the theory of resistive wall modes outlined in Section 2, we need to determine where each discharge fits into the sketch of Fig. 1. This requires the calculation of a single parameter, equivalent to $\hat{r}_w$, that specifies the plasma–wall separation, and a similar single parameter equivalent to $\hat{r}_c$. We adopt the following procedure. First, the PEST ideal stability code [29] is run using experimentally determined plasma profiles and a crescent shaped

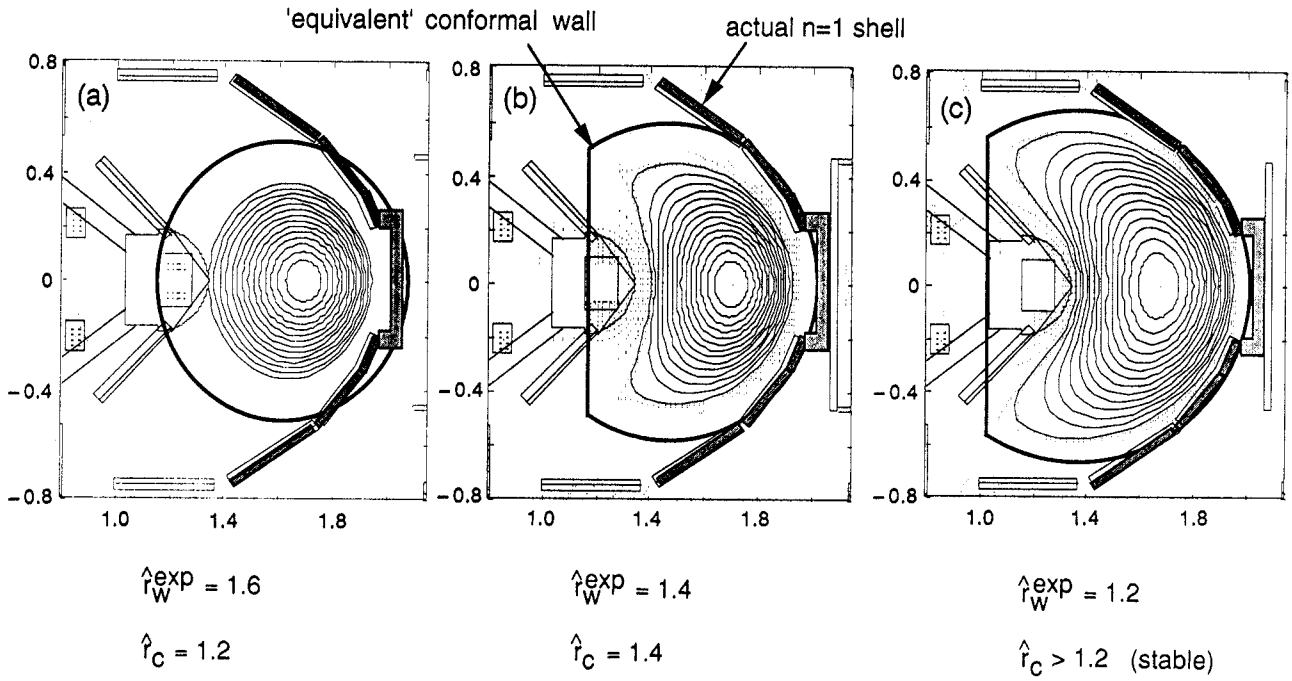

FIG. 3. Flux contour plots of the (a) circular, (b) D-shaped and (c) bean-shaped configurations. The 'equivalent conformal wall', with normalized radius $\hat{r}_w^{exp}$, is calculated using the PEST code, as explained in Section 4.2.

TABLE II. PLASMA-SHELL SEPARATION ALONG SELECTED RADII FOR THE CIRCULAR, D-SHAPED AND BEAN-SHAPED CONFIGURATIONS

	Radius (A)	Radius (B)	Radius (C)	$\hat{r}_w^{exp}$	$\hat{r}_c^{exp}$
Circular	2.09	1.59	1.15	1.6	1.4
D shaped	1.59	1.44	1.17	1.4	1.4
Bean shaped	1.37	1.13	1.15	1.2	>1.2

perfectly conducting wall with a poloidal gap on the midplane [30]; the crescent contour coincides with the actual position of the conducting plates Nos 4 and 5. Next, PEST is run using the same profiles, but with a perfectly conducting wall that completely surrounds the plasma, and whose shape is conformal to the plasma surface. The plasma-wall separation distance is then adjusted so that the external kink growth rate is equal to the value obtained using the crescent shaped wall contour. This defines a wall separation distance we will denote as $\hat{r}_w^{exp}$. Finally, the conformal wall is moved closer to the plasma to find the radius, $\hat{r}_c^{exp}$, at which the external kink is completely stabilized. The values of $\hat{r}_w^{exp}$ and $\hat{r}_c^{exp}$ are analogous to $\hat{r}_w$ and $\hat{r}_c$ used in Fig. 1. They are tabulated for the different plasma configurations in the final two columns of Table II. We see that the circular configurations chosen for the present study correspond to $\hat{r}_w^{exp} > \hat{r}_c^{exp}$, the D-shaped configurations correspond to $\hat{r}_w^{exp} \approx \hat{r}_c^{exp}$, and the bean shaped configurations correspond to $\hat{r}_w^{exp} < \hat{r}_c^{exp}$.

The discharges analysed in this paper were originally produced to study effects other than wall stabilization. For example, the circular and D-shaped plasma configurations were produced to study the dependence of shaping on the onset of fishbone activity [31] while the bean-shaped plasma configurations were produced for the purpose of high-β exploration [23]. We analyse only those discharges that experience disruptions. These

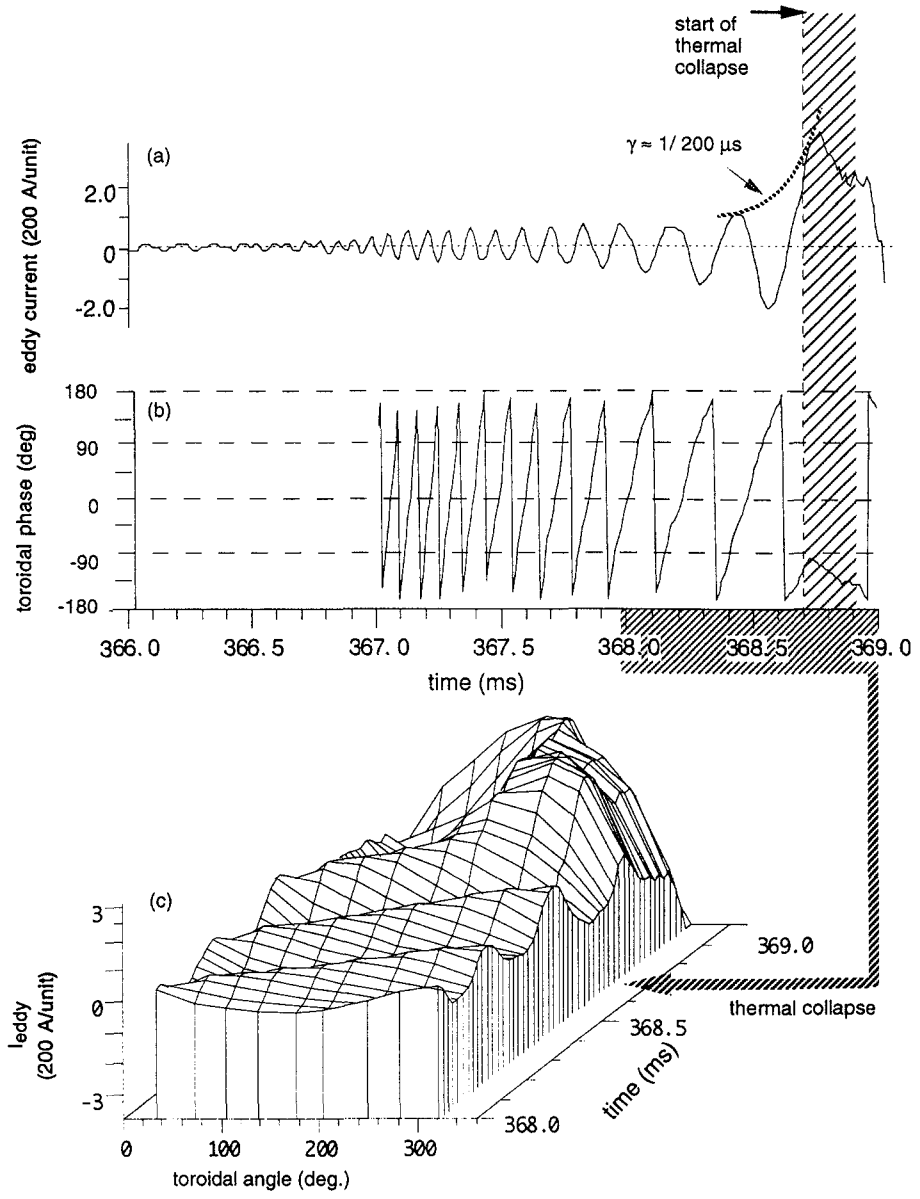

FIG. 4. Time dependence of eddy current disruption precursors for a circular PBX-M discharge: (a) Growing eddy current amplitude at one midplane jumper location. (b) Toroidal phase of the eddy current distribution, $I_{eddy}(\phi,t)$, reconstructed from all ten of the midplane jumpers. (c) The full eddy current distribution, $I_{eddy}(\phi, t)$.

occurred over a wide range of β values during high power NBI heating. The NBI plays two roles; to heat the plasma and raise β, and to induce and maintain plasma rotation.

4.2. Circular plasmas

A typical precursor of the disruption phase of a nearly circular PBX-M discharge is shown in Fig. 4. Such precursors always show rapid mode rotation and fast growth rates. The plasma parameters are: B_t = 1.14 T, edge safety factor q_{edge} = 2.4, β = 1.5%, β_p = 1.8, I_p = 180 kA, a = 0.29 m and κ = 1.2. MSE measurements (averaged over multiple shots) show $q(0) \approx 0.8$.

Figure 4(a) shows the eddy current signal measured on one midplane connection jumper during the 2.5 ms interval immediately prior to the major thermal collapse. The precursor eddy current magnitude grows with a

time constant of 150 to 200 μs, approximately 10 times the poloidal Alfvén time, to a maximum of 1 kA at the start of the thermal collapse. The perturbed magnetic field at the shell consistent with 1 kA of eddy current can be estimated as 60 G, or 5% of the equilibrium edge poloidal field.

Figure 4(c) shows the evolution of the eddy current distribution, $I_{eddy}(\phi, t)$, determined from measurements at all ten of the midplane jumpers. At a fixed time, the mode structure is $n = 1$ and the propagation direction is the same direction as the parallel NBI. Figure 4(b) shows the time evolution of the toroidal phase of $I_{eddy}(\phi, t)$. The observed frequency is rapid, and is seen to decrease from 10 kHz (comparable to the steady state central plasma rotation frequency) to 3 kHz as the mode grows, and changes sign during the thermal collapse. The phase evolution during the slowing-down stage is not pure sinusoidal, indicating an influence (albeit weak) of the resistive wall on the MHD mode.

Bursts of fishbone activity were observed prior to the disruption phase shown in Fig. 4. The fishbones occur at 2 to 3 ms time intervals, and have typical growth times of 200 μs, comparable to the eddy current growth time. The fishbones are first detected in this discharge when β exceeds 1.3%, at $t = 340$ ms. This value of β is found to agree well with the β limit for internal kink modes predicted by the PEST stability code. The marginally unstable internal kink eigenfunction shows a radially localized mode structure dominated by the $m/n = 1/1$ component (m and n are the poloidal and toroidal mode numbers, respectively). As β is increased, PEST calculations show that the $m/n = 1/1$ component remains large; however, the relative magnitudes of the $m/n = 2/1$ and 3/1 modes increase and the mode develops a mixture of external plus internal character.

For the circular PBX-M discharges, the PEST code calculates an effective wall radius (see previous section) of $\hat{r}_w^{exp} \approx 1.65$, and a critical wall radius of $\hat{r}_c^{exp} \approx 1.20$. From the discussion in Section 2, we see that the PBX-M circular plasmas lie in the ideal unstable, weak plasma-shell coupling regime, with $\hat{r}_w > \hat{r}_c$ in Fig. 1. In this regime, the growth rate is predicted to be on the Alfvén time-scale, and the mode frequency is predicted to be comparable to the plasma rotation frequency. These predictions are in agreement with the experimental data.

4.3. D-shaped plasmas

The plasma parameters for D-shaped configurations are: $\kappa = b/a = 0.55$ m/0.3 m (=1.83), $\delta \approx 0.8$–1.0, indentation $\lesssim 5\%$ (i.e. negligible bean shaping), $\beta = 2.2\%$, $\beta_N \equiv \beta/(I/aB_t) = 4.0$, $B_t = 1.0$ T and $q_{95} \approx 3.9$. The MSE measurements show shot averaged, $q(0) \approx 0.8$, for the safety factor at the plasma magnetic axis. The increased plasma elongation compared with circular plasmas leads to a more effective coupling of the plasma to the conducting shell.

In these experimental conditions with low $q(0)$, yet high triangularity, ideal MHD calculations using PEST with a perfectly conducting wall on the plasma surface show that low-n internal modes are marginally unstable. With a conducting wall at the actual location of the PBX-M shell, the low-n external modes calculated by PEST are also marginally unstable, and retain a strong internal character with a substantial $m/n = 1/1$ component near the centre. The calculated growth rates are 30 to 50% of the calculated values with the wall at infinity. The effective wall separation distance and the critical stabilizing wall distance are calculated to be $\hat{r}_w^{exp} \approx \hat{r}_c^{exp} = 1.4$. With reference to the resistive wall mode diagram, Fig. 1, the PBX-M D-shaped plasmas therefore correspond to a weak plasma–shell coupling regime with $\hat{r}_w \gtrapprox \hat{r}_c$, but close to the region of transition to strong coupling.

Two examples of disruptions in these weakly coupled D-shaped plasmas are shown in Figs 5 and 6. The first example, shot 273 290, is a case where the toroidal mode frequency is essentially zero during the precursor phase. Figure 5(a) shows the eddy current evolution at one of the midplane junction bars, and Fig. 5(b) shows the amplitude of the $n = 1$ component of the full eddy current profile $I_{eddy}(\phi, t)$. An $n = 1$ precursor grows with a short time constant of $\gamma^{-1} \approx 350$ μs, beginning at $t \approx 497.5$ ms. The toroidal phase evolution, Fig. 5(c), shows that although the precursor initially rotates, the mode locks at the toroidal location $\phi \approx -50°$ and remains locked until the start of the thermal collapse at $t = 498.7$ ms. (Note that for $t \lesssim 498$ ms, the phase measurement is unreliable since the mode amplitude is so small.) The $n = 1$ amplitude saturates within 300 to 400 μs of initiation, and remains saturated for $\Delta t \approx (1\text{–}2)\gamma^{-1}$. Figures 5(d) to (f) show soft X ray signals detected at the plasma centre, at one half of the minor radius and at the plasma edge. The mode is seen to have a significant radial extent, indicating that the mode is global, in agreement with the PEST calculations.

The Mirnov signal in Fig. 5(g) shows excitation of fishbone instabilities with a 2 to 3 ms interval between bursts. An interesting observation is that sometimes the fishbone is active when a stationary $n = 1$ external mode

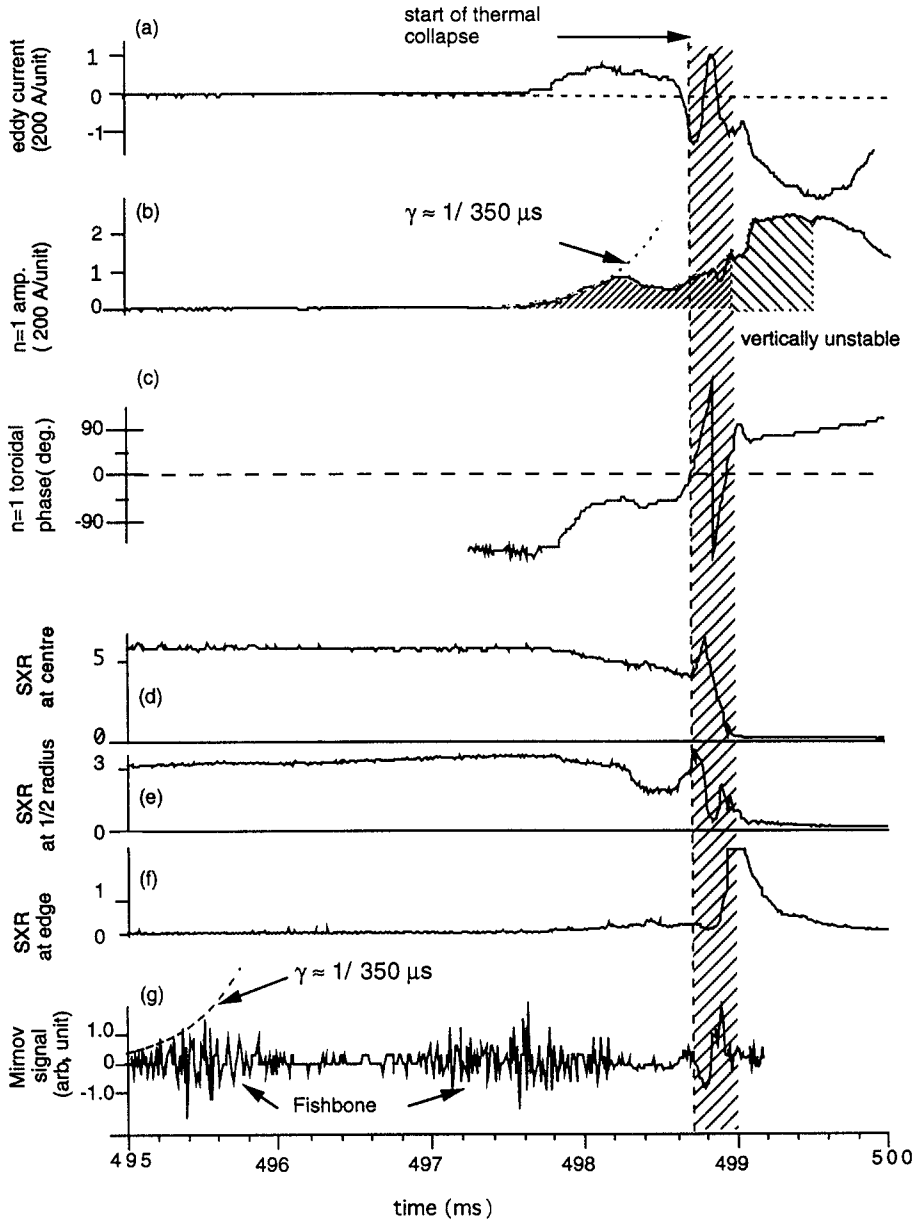

FIG. 5. A non-rotating n = *1 precursor for the D-shaped PBX-M discharge 273 290. (a) Evolution of eddy current at one midplane location. (b) Amplitude evolution of* I_{eddy} (ϕ,t) *reconstructed from all of the midplane jumpers. (c) Toroidal phase evolution of* I_{eddy} (ϕ,t). *(d) to (f) Soft X ray signals from the plasma centre, one half of the minor radius and from the plasma edge. (g) Mirnov signals showing fishbone oscillations.*

starts to grow (e.g., the second fishbone burst in Fig. 5(g)). This indicates that a 'laboratory frame' $n = 1$ external kink mode can be excited simultaneously with a 'plasma frame' $n = 1$ fishbone mode.

Returning to the eddy current amplitudes in Figs 5(a) and (b), there is no significant increase in amplitude just before the onset of the final thermal collapse. This indicates that some trigger other than the existing $n = 1$ mode is ultimately responsible for the final β collapse. On the other hand, all major disruptions observed so far on PBX-M show some kind of $n = 1$ precursor. The $n = 1$ precursor is always necessary, but its existence is not a sufficient condition for disruption.

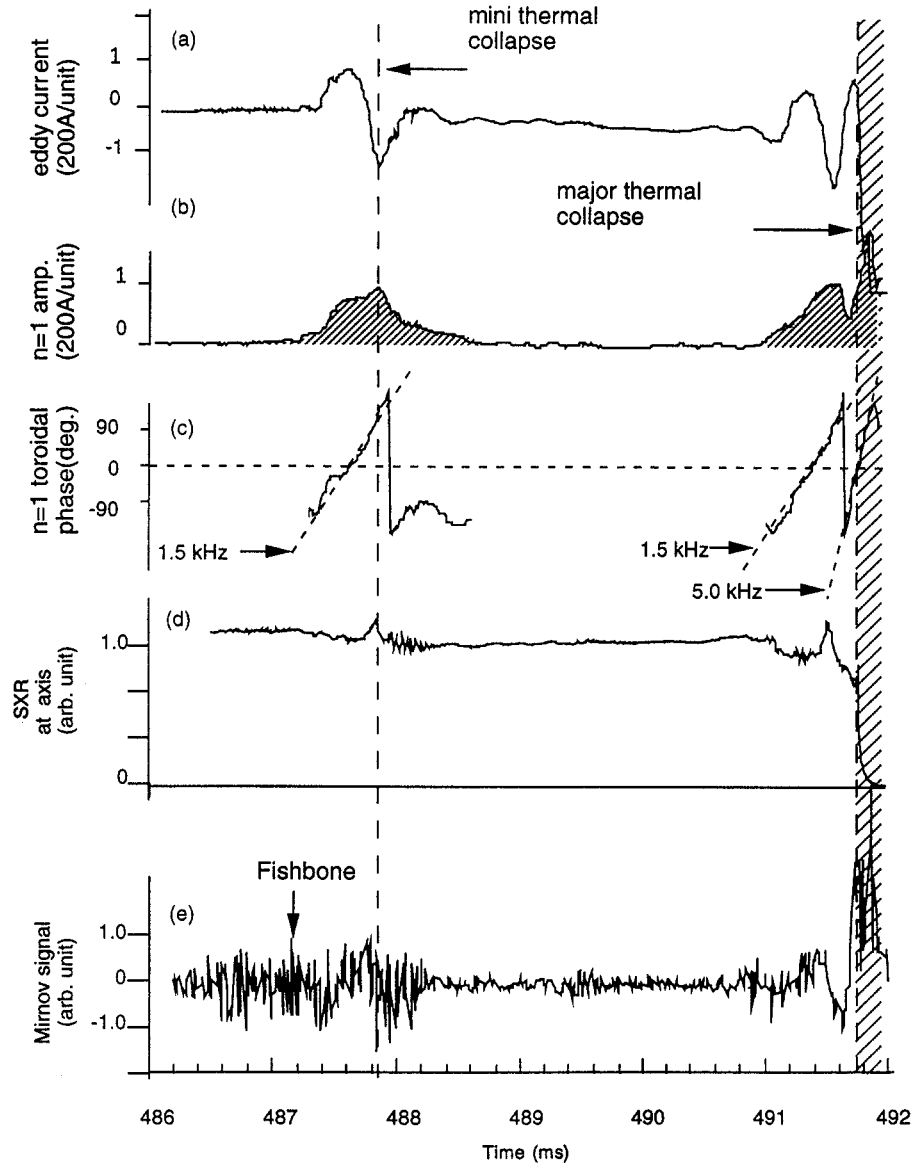

FIG. 6. Disruption precursor for D-shaped PBX-M discharge 273 250. Here, the precursor is a rotating n = *1 mode.*

During the thermal collapse period (indicated by the shaded time domain shared by each of the plots), the $n = 1$ mode starts to rotate toroidally. The $n = 1$ structure is well preserved until the completion of the thermal collapse (shown as $t = 499.00$ ms $\pm$ 20 μs by the soft X ray signal) when loss of position control results in a vertical instability. There is no indication of the excitation of modes with $n > 1$, indicating that the thermal collapse does not require the collapse of the $n = 1$ magnetic island, leading to stochasticity.

A second example of a weakly coupled D-shaped plasma disruption (shot 273 250) is shown in Fig. 6. The mode growth time in this example is comparable to that of the previously described shot 273 290; however, the precursor is a rotating mode. A precursor is first observed in the eddy current pattern at $t = 487.2$ ms. The mode grows with a time constant of $\gamma^{-1} \approx 200$ μs, then saturates. At $t = 487.8$ ms, a mini thermal collapse is detected by the soft X ray signal, and this is followed by a slow decay of the eddy current amplitude. Up to the

mini collapse, the toroidal mode rotation was sustained at $\omega/2\pi \approx 1.5$ kHz (corresponding to a mode velocity of 15 km/s and comparable to the plasma rotation velocity at the plasma edge). After the mini thermal collapse, the mode amplitude decreases and the mode rotation slows and eventually locks. Before the mini thermal collapse the soft X ray data show the $n = 1$ mode had significant $m = 1$ and $m = 3$ components. After the mini collapse, the mode structure was predominantly $m/n = 3/1$, with no 1/1 contribution. The change in mode structure is presumably due to a change in $q(0)$.

At $t = 491.0$ ms, a second rotating $n = 1$ mode was detected by the eddy current signal, the growth of which led to the major thermal collapse. Soft X ray data show that the mode is predominantly $m/n = 1/1$ with some additional 3/1 contribution. The toroidal rotation frequency of the mode during its initiation is $\omega/2\pi \approx 1.5$ kHz, similar to the frequency of the mini collapse precursor. This time, however, the mode rotation rate increases to approximately 5 kHz as the final thermal collapse is approached. The low frequency precursors for the D-shaped plasmas are in striking contrast with the large rotation frequencies observed for the circular plasma disruptions (see Fig. 4). We also note that the mode rotation rate for the circular plasma disruption precursor decreases prior to the major thermal collapse, whereas the rotation rate for the D-shaped plasma precursor increases. The observation of disruption precursors with varying mode frequency is consistent with the resistive wall mode theory predictions displayed in Fig. 1: there, we see that for configurations with $\hat{r}_w \approx \hat{r}_c$ the mode frequency can increase or decrease depending on profile changes that can make $\hat{r}_w$ closer to or further from $\hat{r}_c$.

4.4. Bean-shaped plasmas

Bean-shaped plasmas in PBX-M have the closest proximity between the the plasma surface and the conducting plate assembly (see Table II and Fig. 3). For these configurations we can expect to find the strongest plasma–shell coupling, and the strongest influence of the conducting shell on MHD behaviour.

Figures 7 and 8 show disruption precursors for a bean-shaped configuration, shot 273 849. The plasma parameters at the time of the thermal collapse at $t = 450$ ms were: $\beta = 2.7\%$, $\beta_p = 0.83$, $I_p \approx 540$ kA, $B_t = 1.25$ T, $\beta_N = \beta/(I_p/aB_t) = 1.9$ and $q_{95} \approx 3.7$. MSE measurements were not available for determining $q(0)$. However, the best match between observed flux values and those from equilibrium reconstruction was obtained using $q(0) = 0.9$. PEST analysis shows that the internal kink mode is stable, despite $q(0) < 1$, owing to the strong bean shaping and high triangularity of the flux surfaces near the magnetic axis [32].

Figure 7(a) shows the time dependence of the eddy current in one of the 10 midplane connection jumpers, while Figs 7(b) and (c) show the amplitude and phase of the $n = 1$ component of the full eddy current distribution obtained from all 10 of the midplane jumpers. At $t \approx 385$ ms a non-rotating precursor grows with $\gamma \approx 1/5$ ms. Figure 7(d) shows the evolution of plasma β, calculated by equilibrium reconstruction, and its relationship to β_c^∞, the critical β for marginal stability of $n = 1$ ideal external kink modes calculated by PEST with a perfectly conducting wall at infinity. We see that the initial growth of the precursor is correlated with the time at which β first exceeds β_c^∞. After a short period of growth, the mode begins to rotate with a rapid toroidal rotation frequency of 3 to 5 kHz. During the transition to a rotating state, no discontinuities are observed in the time derivative of the eddy current pattern, $I_{eddy}(\phi, t)$, and we conclude that the rotating mode is a continuation of the existing non-rotating mode, rather than some other newly triggered mode (such as a tearing mode). Coincident with the mode rotation is a substantial decrease in mode amplitude. Finally, when the mode amplitude is small, the mode ceases to rotate. The cycle of mode growth, followed by mode rotation and mode amplitude decrease, occurs several times before the final phase of mode growth begins at $t \approx 430$ ms. The mode is essentially non-rotating, and has a growth rate of $\gamma \approx 1/15$ ms.

Figure 8(a) shows the time behaviour of the toroidal eddy current distribution, $I_{eddy}(\phi, t)$ for $t > 430$ ms until the beginning of the thermal collapse. The $n = 1$ mode is seen to lock at a certain toroidal angle. Analysis of many high-β, low-q disruptions for bean-shaped plasmas in PBX-M shows mode locking at preferred toroidal angles in the range of $\Delta\phi = \pm 60°$ from the toroidal ohmic gap location. The preferred angle may be due to the toroidal asymmetry due to the ohmic gap, or to other asymmetries due to field errors associated with the poloidal field coil system. So far, no systematic survey of residual field errors has been carried out in PBX-M.

Full tomography was not available for the accurate reconstruction of the internal mode structure from experimental data. However, information on the internal mode structure of the quasi-stationary precursor mode leading to the final thermal collapse is obtained by

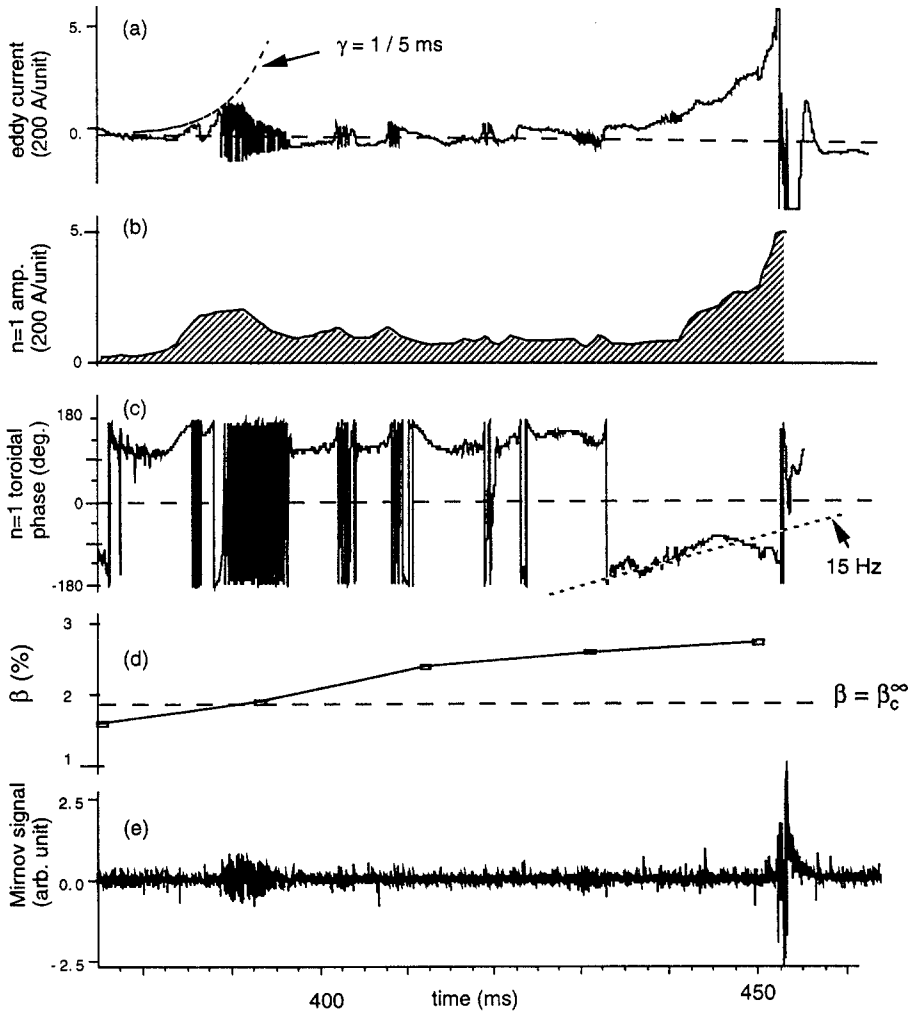

FIG. 7. Disruption precursor for the bean-shaped PBX-M discharge 273 849. (a) to (c) Evolution of the eddy current. (d) Evolution of plasma β, and its relation to β_c^∞, the β limit for n = *1 kinks calculated by PEST with a conducting wall at* ∞. *(e) Mirnov signals.*

measuring the slow change of the vertically measured soft X ray intensity profile, $S(z, t)$. Figure 8(b) shows $S(z = \pm 13$ cm, $t)$ at $\phi = 0$. The two signals are similar up to $t = 430$ ms, then slowly deviate from each other, indicating the development of a z asymmetry. The asymmetry builds up on a time-scale of ≈ 20 ms, similar to the time-scale of the mode growth shown in Fig. 8(a).

The time development of the difference of the soft X ray profile relative to the profile at $t_0 = 430$ ms, $\Delta S(z, t) = S(z, t) - S(z, t_0)$, is shown in Fig. 8(c). The profile change can be decomposed into symmetric and antisymmetric components, $\Delta S_{\text{sym}}(z, t)$ and $\Delta S_{\text{asym}}(z, t)$, respectively. The symmetric component corresponds either to an even-m perturbation or to a change in the equilibrium pressure profile. The antisymmetric component reflects the development of either an $n \neq 0$, odd-m perturbation, or of an $n = 0$ vertical plasma motion. As was discussed in Ref. [27], an $n = 0$ mode induces a saddle current pattern on the conducting shell, uniquely characterized by a polarity change in I_{eddy} between the toroidal gap at $\phi = +0$ and $-0(2\pi)$. By analysing $I_{\text{eddy}}(\phi, t)$, such as in Fig. 8(a), it is possible to distinguish the $n = 0$ mode from other n.

Figure 8(d) shows $\Delta S_{\text{asym}}(z, t)$ normalized by the gradient of $S(z, t)$, $\xi_r = \Delta S_{\text{asym}}(z, t)/(\partial S/\partial z)$, to illustrate the observed displacement vector of the mode. The displacement obtained in this way must be regarded as approximate since the X ray signals are integrated along

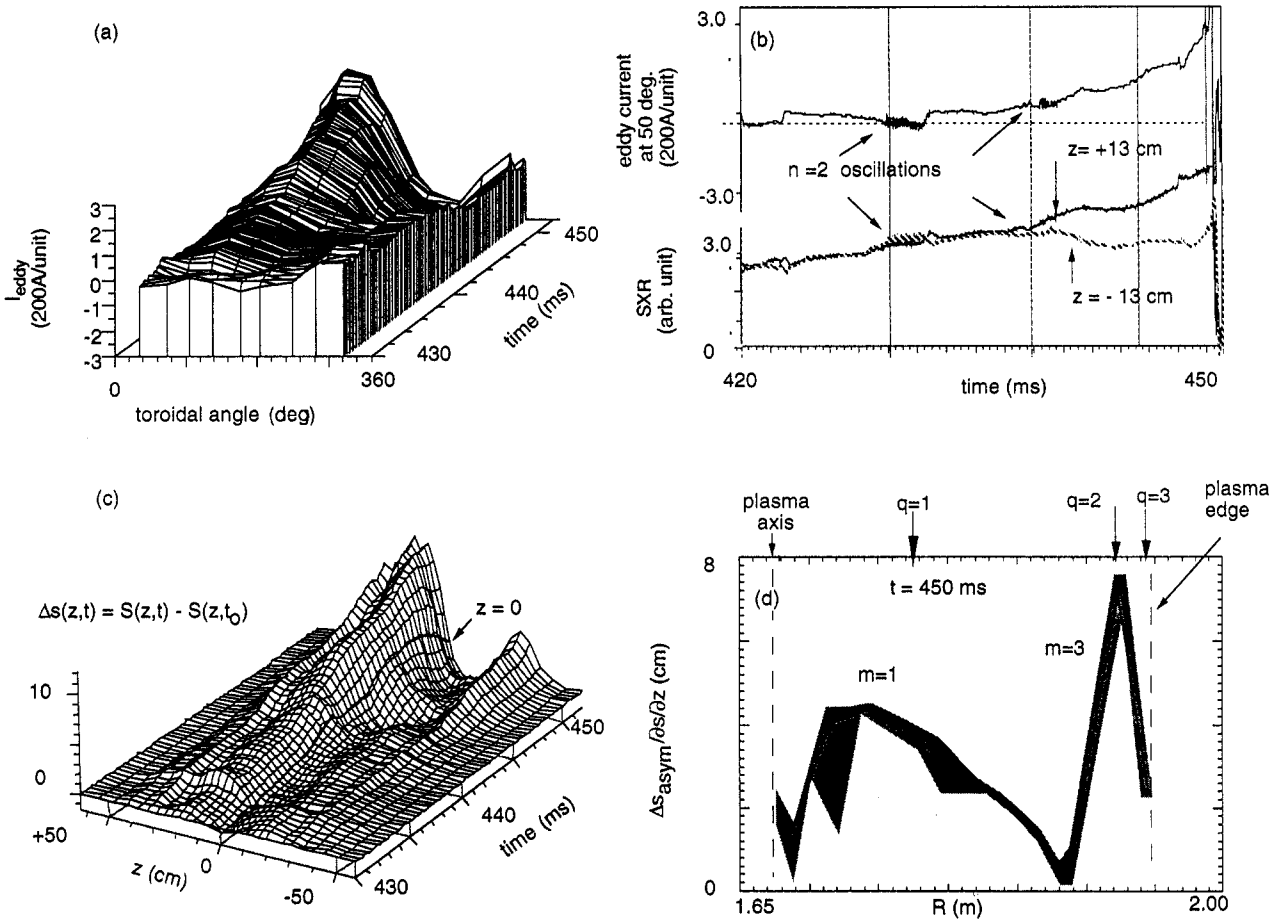

FIG. 8. Disruption precursor for bean-shaped PBX-M discharge 273 849. (a) n = *1 toroidal eddy current pattern,* $I_{eddy}(\phi,t)$. *(b) Eddy current signal measured at* $\phi = 50°$ *and soft X ray signal. (c) Soft X ray* z *profile perturbation* $\Delta S(z,t) = S(z,t) - S(z,t_0)$. *(d) Radial structure of* n = *1 mode;* $\xi_r = \Delta S_{asym}/(\partial S/\partial z)$.

the line of sight over the perturbation. The locations of q values indicated in the figure are determined from equilibrium reconstruction and help identify the m values labelling the peaks in the ξ_r profile. The observations are seen to indicate that the stationary $n = 1$ perturbation leading to the final thermal collapse is a global mode with a large odd-m component, predominantly $m = 1$, $n = 1$ and $m = 3$, $n = 1$. The magnitude of the symmetric component, $\Delta S_{sym}(z, t)$, even at its maximum value, was 30 to 50% of the magnitude of the asymmetric component, $\Delta S_{asym}(z, t)$, indicating that the $m = 2$ component of the displacement eigenfunction is weaker than the $m = 1$ component. These observations suggest that the mode is a globally driven external kink mode dominated by $m/n = 1/1$ rather than a resistive mode excited near the $q = 2$ surface.

Figure 8(b) shows interesting evidence that rotating and non-rotating MHD modes can be simultaneously excited. Superimposed on the quasi-stationary $n = 1$ mode is a 4 kHz oscillation at $t = 430$ ms (seen particularly clearly in the eddy current signal) and a somewhat weaker ~3 kHz oscillation at $t = 440$ ms. The eddy current pattern and soft X ray signal shows a dominant single $n = 2$ component with $m = 4$. These oscillatory modes were localized off-axis, at a radius of about 30 cm.

Profiles of ion temperature, $T_i(R)$, and plasma toroidal rotation, $v_\phi(R)$, are shown in Figs 9(b) and (c), for three different time values. To set a scale for the plasma rotation velocity, Fig. 9(b) also shows the ion sound speed profile, $C_s(R)$. The outboard plasma edge is located at a major radius of $R = 1.94$ m. However, the temperature and velocity profile measurements are

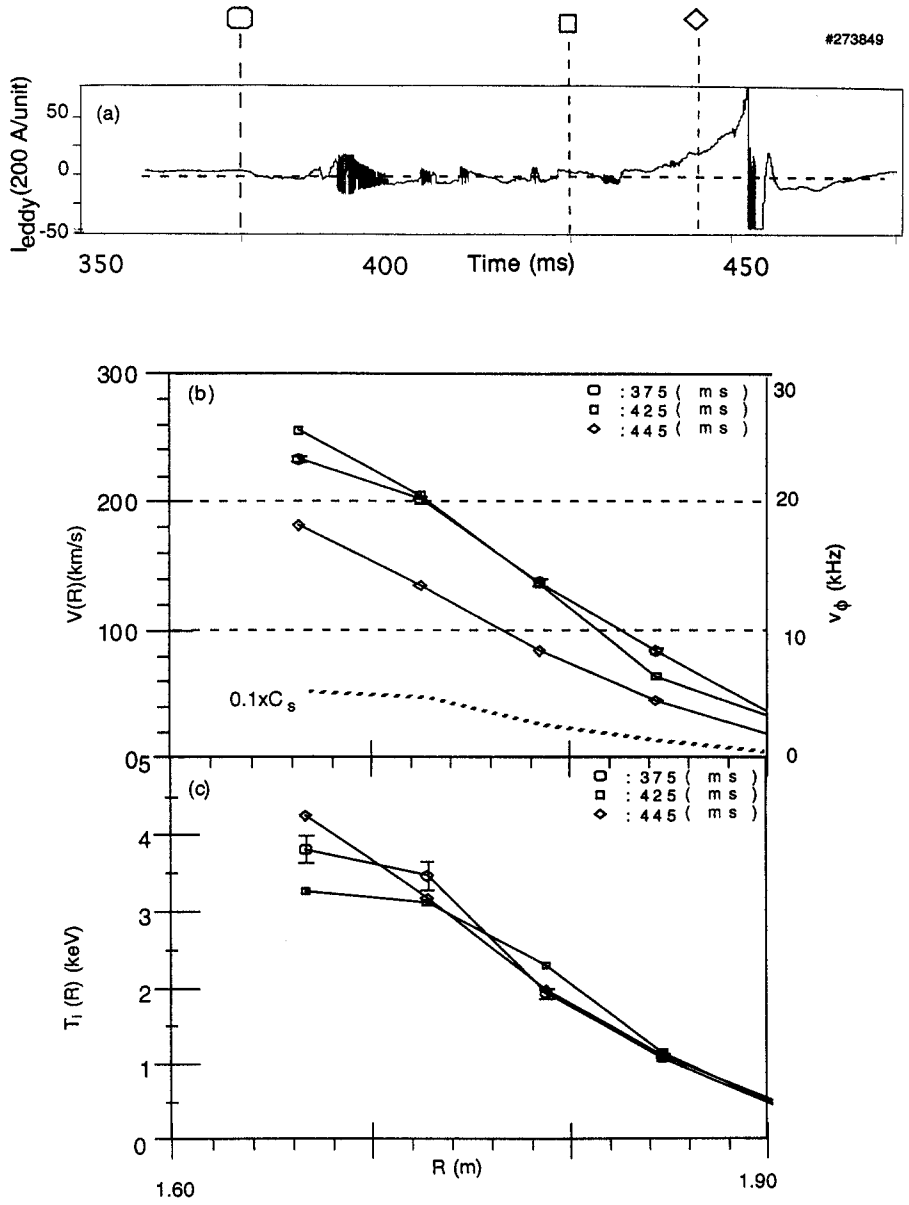

FIG. 9. (a) Evolution of eddy current showing time values at which profile measurements are displayed. (b) Velocity profile, v_ϕ(R), (solid lines) obtained at t = *375, 425 and 445 ms. The ion sound speed profile, 0.1 C_s(R), is shown as a dashed curve. (c) Ion temperature profile measured at* t = *375, 425 and 445 ms.*

obtained only to a radius of R = 1.90 m, approximately the radius of the q = 3 surface. The observed central $T_i(0) \approx 4.5$ keV and $v_\phi(0) \approx 250$ km/s are typical for PBX-M shots at high β [23]. In spite of the excitation of the n = 1 mode, the change in $T_i(r)$ is modest. The toroidal rotation velocity is seen to decrease substantially between t = 425 ms and t = 445 ms, approximately the same time as the beginning of the final mode amplitude increase leading to the thermal collapse. The 'edge' rotation velocity, $v_\phi(q \approx 3)$, decreases from 30–40 km/s to 20 km/s corresponding to the toroidal rotation frequency, $\Omega/2\pi$, decreasing from 3–4 kHz to 2 kHz (the circumference along the major radius is $\approx$ 10 m).

During the time interval from t = 375 ms until the final thermal collapse, PEST calculations with a per-

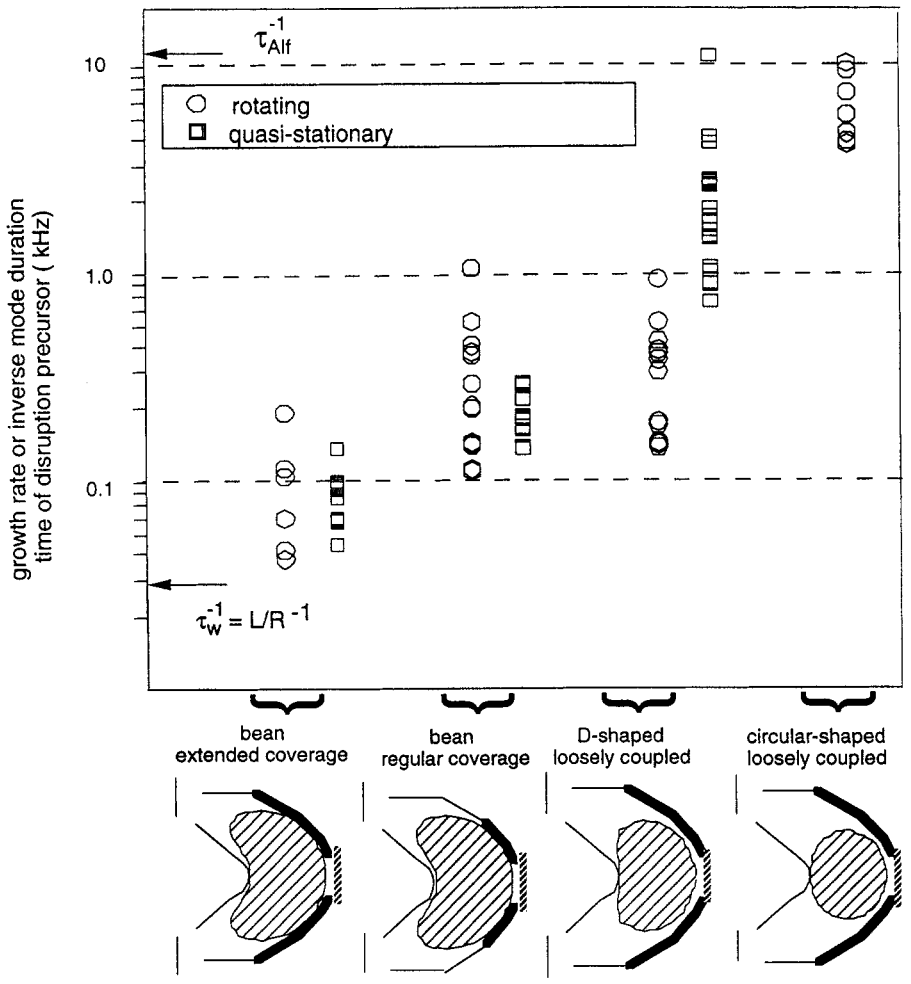

FIG. 10. Mode growth rate, or inverse mode duration time, for circular, D-shaped and bean-shaped PBX-M disrupting plasma configurations. The variation of mode duration from MHD time-scales to the L/R *time-scale of the conducting shell is correlated with the plasma-shell coupling strength.*

fectly conducting wall at the location of the PBX-M conducting shell show the plasma to be stable with respect to ideal $n = 1$ external kink modes. It follows from Fig. 7(d) that the plasma parameters for $t > 375$ ms correspond to $\hat{r}_w < \hat{r}_c$. It follows from the discussion in Section 2, and from Fig. 1, that the bean-shaped configuration lies either in the transition region between weak and strong plasma–shell coupling, or in the strong plasma–shell coupling regime. The observed change in mode behaviour between quasi-stationary ($\omega/\Omega \ll 1$) and rotating states is therefore consistent with resistive wall mode theory, since small changes in plasma profile can be expected during the instability, which lead to small changes in $\hat{r}_w$ relative to $\hat{r}_c$. In Section 5, we will present a detailed numerical calculation of the resistive wall mode stability of shot 273 849 using the NOVA-W stability code.

4.5. Dependence of mode duration on shell coupling

Figure 10 shows a summary of mode duration, Δt ($\sim$ growth time γ^{-1}), for PBX-M disrupting plasmas for the variety of configurations discussed in Section 4.1. The different couplings were obtained primarily by varying the plasma shape. The data are grouped into four sets corresponding to: (a) circular plasmas (as discussed in Section 4.2), (b) D-shaped

plasmas (see Section 4.3), (c) bean-shaped configurations where the electrical connection between plates Nos 4 and 5 is open so that only plate No. 5 can support stabilizing helical eddy currents ('regular' shell coverage) and (d) bean-shaped configurations that use the 'extended' shell coverage provided by the combined plates Nos 4 and 5 (discussed in Section 4.4). In all cases, the precursors were triggered during high-β, low-q exploration with $B_t \approx 1.0$–1.3 T. To provide $q_{95} \lesssim 4$, the different plasma shapes carry different total plasma current.

Precursors are classified as either rotating or quasi-stationary depending upon their behaviour just before the thermal collapse. Modes that were initially non-rotating but which change to rotating prior to the thermal collapse are categorized as rotating. Behaviour during the thermal collapse is not taken into account for this categorization.

For discharges where exponential growth of the mode amplitude was clearly identified, as in the case of the circular discharge shown in Fig. 4, the growth rate is plotted in Fig. 10. In other cases, such as the D-shaped discharges shown in Figs 5 and 6, where there is no obvious linear growth rate behaviour, the mode duration time is plotted.

All circular plasmas led to rotating precursors, an example of which was shown in Fig. 4. For the D-shaped plasmas, about 55% were non-rotating. For bean-shaped plasmas with regular shell coverage, 50% were non-rotating, and for those with extended shell coverage, 75% were non-rotating.

As shown in Fig. 10, precursors of circular weakly coupled configurations have growth rates $\gamma_{n=1} \sim \gamma_{Alf}$, and growth rates decrease to the inverse L/R time-scale of the passive plates as the plasma–shell coupling is increased.

5. NOVA-W calculation of resistive wall mode stability

In this section, the NOVA-W linear stability code [14] is used to determine the effect of toroidal rotation on the resistive wall mode stability of shot 273 849, a bean-shaped configuration with strong plasma–shell coupling. For this strongly indented configuration, the ideal internal kink is robustly stable, a favourable condition for producing slowly growing resistive wall modes. A description of the disruption precursors for shot 273 849 was presented in Section 4.4.

A requirement for the excitation of resistive wall modes is that a low-n external kink mode should be unstable in the absence of any conducting wall, but stable in the presence of a perfectly conducting wall at the location of the actual conducting wall. Thus, from the data shown in Fig. 7(d), the resistive wall modes may be present only for times $t \gtrsim 375$ ms when the ideal kink mode becomes unstable.

The NOVA-W code [14] accurately models the geometry and conductivity of the poloidally segmented conducting shell in PBX-M. All poloidal elements shown in Fig. 2 are included. Since NOVA-W examines the linear stability of axisymmetric equilibria perturbed by a single toroidal mode number, n, the non-axisymmetric elements of the PBX-M conducting shell, such as the midplane electrical jumper and the toroidal gap, were not included in the model. In the absence of midplane jumpers, the numerical results represent a configuration where the plasma–shell coupling is weaker than the true coupling.

In the present analysis, the plasma rotation is treated as a rigid body rotation, and simulated by rotating the wall [13, 14]. This simplification allows us to treat the equilibrium as static, and separate the effects of wall stabilization from other equilibrium modifications due to plasma rotation. Chu et al. [16] have compared resistive wall mode growth rates for a uniformly rotating plasma with those of a plasma with sheared rotation and found that, at least for the case of a single rational surface in the plasma, the bulk plasma rotation frequency at the rational surface is much more important than the rotation shear in determining the stability of the resistive wall mode. The MHD equilibrium for the present analysis was prepared, consistent with the experimental profiles corresponding to $t > 375$ ms. The plasma toroidal rotation velocity was treated as a variable input parameter in the calculations so that an exploration could be made of how close the experimental conditions were to achieving complete stability of the resistive wall mode by plasma rotation. Further details of the MHD model assumed in NOVA-W can be found in Ref. [14].

Figure 11 shows a plot of the real and imaginary parts of the $n = 1$ eigenfrequency calculated by NOVA-W, as a function of assumed toroidal rotation velocity, v_ϕ. The solid curve represents the calculated mode frequency, $f = \mathrm{Re}(\omega)/2\pi$; the dashed curve represents the calculated growth rate, $\gamma = \mathrm{Im}(\omega)$. Without plasma rotation, i.e. $v_\phi = 0$, the calculated resistive wall mode growth rate is $\gamma = 1/44$ ms, which is close to the value of the inverse L/R time calculated by the 3-D SPARK code [28]. As v_ϕ is increased the plasma

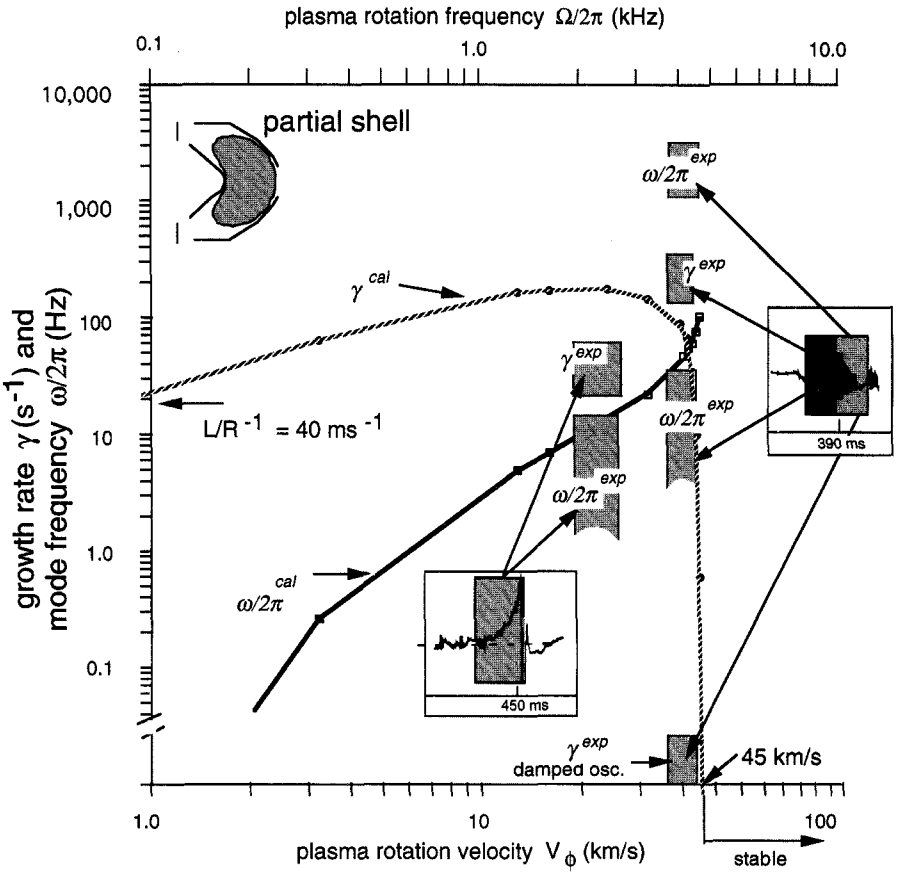

FIG. 11. NOVA-W code predictions of the dependence of growth rate, γ (dashed line) and mode frequency, f = $\omega/2\pi$ (solid line), on the assumed plasma rotation velocity, v_ϕ. The plasma equilibrium is a fit to the bean-shaped configuration 273 849 whose disruption precursors were documented in Figs 7 to 9. Using the actual segmented conducting shell in PBX-M, a rotation velocity of 45 km/s completely stabilizes the external kink mode. The actual rotation velocities in the experiment are in the range from 20 to 40 km/s. Experimental values of γ and f for t $\approx$ 390 ms and t $\approx$ 450 ms are shown as boxed regions.

rotation initially feeds energy to the instability, causing an increase of the growth rate. A maximum $\gamma \approx$ 1/5–1/6 ms is obtained for $v_\phi \approx$ 20 km/s. With higher rotation velocity, the growth rate decreases, and the mode is completely stabilized for $v_\phi > v_\phi^{crit} = 45$ km/s, equivalent to a rotation frequency of $\Omega/2\pi \approx 4.5$ kHz. The mode frequency is nearly zero at low rotation velocity and increases to approximately 100 Hz when the kink mode becomes marginally stable. The required rotation velocity, v_ϕ^{crit}, is 1% of the Alfvén speed at the plasma centre, or about 10% of the central ion sound speed.

We compare NOVA-W calculations with experimental results using eddy current measurements obtained during the two major events shown in Fig. 7(a); namely, the period of mode growth followed by damped oscillation near t = 390 ms, and during the final mode growth immediately prior to the thermal collapse near t = 450 ms. Following the notion that sound wave damping at resonant surfaces near the plasma edge governs the stabilization of β-driven resistive wall modes, the experimental growth rates and mode frequencies in Fig. 11 are associated with experimental values of v_ϕ taken at R = 1.90 m, approximately the radius of the $q = 3$ surface. From Fig. 7(b), we see that $v_\phi \approx 40$ km/s at $t \approx$ 390 ms, and $v_\phi \approx 20$ km/s at $t \approx$ 450 ms.

In Fig. 11, the shaded box regions show the growth rate and mode frequencies for both the quasi-stationary and rotating precursor stages near $t \approx$ 390 ms, and for the quasi-stationary precursor observed at $t \approx$ 450 ms. An upper bound for the experimental mode frequency

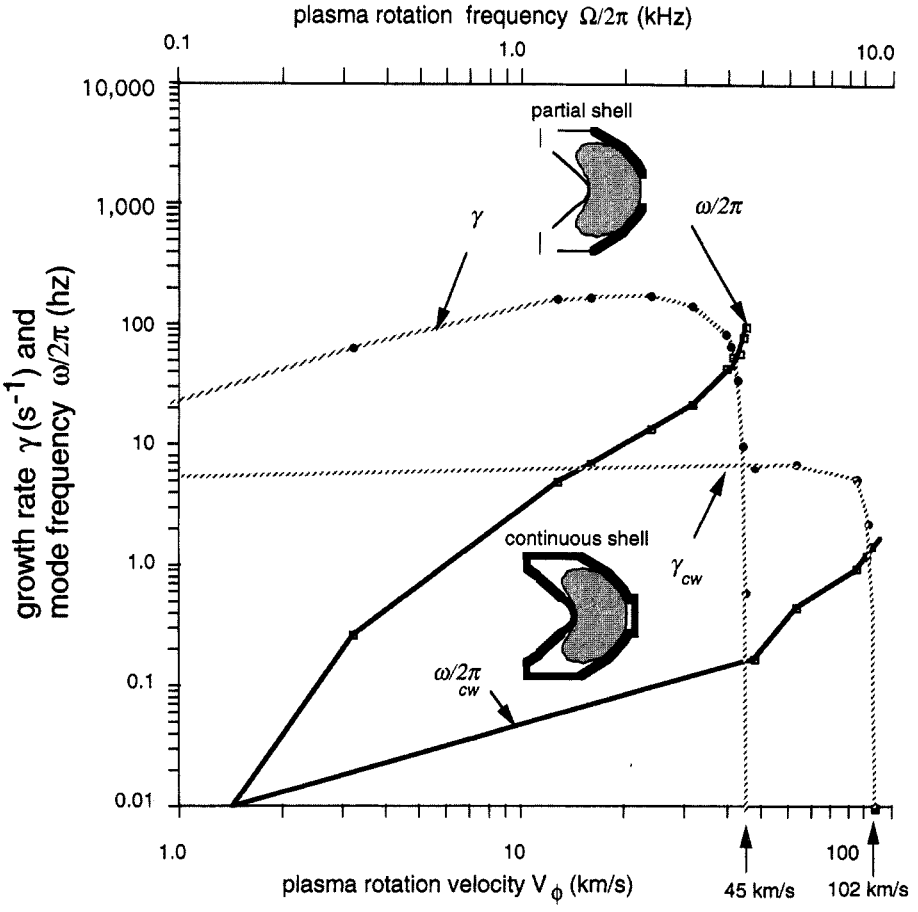

FIG. 12. Growth rate, γ and mode frequency, f, calculated by NOVA-W, comparing partial and continuous shell coverage.

prior to the major thermal collapse is obtained by noting that the time interval during which monotonic mode growth is observed is about 15 ms. Assuming there is a maximum of one quarter of a period of (undetected) mode oscillation during this interval, an upper bound on the experimental mode frequency is f = 15 Hz. The lower bound for f is zero. Similar bounds for f can be calculated for the quasi-stationary growth period near t = 390 ms. We note the qualitatively good agreement between the observed and calculated values of f and γ.

An interesting feature of resistive wall mode theory is the predicted dependence on plasma–wall geometry of the critical rotation velocity required for complete stability. It has been argued that to minimize the required v_ϕ^{crit} for achieving complete stability, one should operate with a resistive wall placed as close as possible, but inside, the critical wall location at which an ideal wall is able to stabilize the external kink. Such a configuration allows rapid toroidal rotation of the eddy current pattern and inhibits flux leakage through the resistive wall. For PBX-M it turns out that if the gaps in the existing poloidally segmented conducting plates are filled with conducting material of the same thickness and conductivity as the actual plates, thereby making the conducting shell poloidally continuous and with a longer L/R time constant than the actual shell structure, this fictitious shell would be *less* efficient for stabilizing resistive wall modes than the actual shell system. In Fig. 12, we compare the values of γ and f obtained by NOVA-W using the (actual) poloidally segmented conducting shell with values obtained using a fictitious poloidally continuous shell with no poloidal gaps. Here, the fictitious continuous shell geometry is a closed shell that passes through and connects each of the passive plates shown in Fig. 2. As expected, the growth rate for the case of zero plasma rotation frequency is smaller for the continuous shell than it is for the poloidally segmented shell. This simply reflects the fact that there is

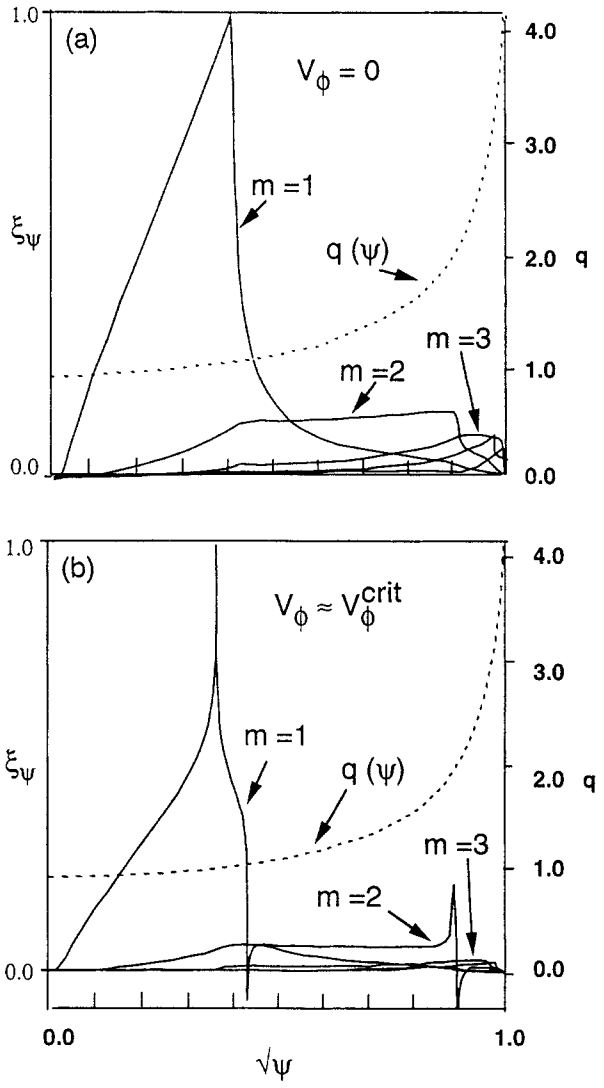

FIG. 13. NOVA-W eigenfunctions for the resistive wall external kink modes for the cases of (a) zero rotation velocity, and (b) a rotation velocity close to the conditions required for marginal stability. For the latter case, significant sound wave damping near the rational q *surfaces is seen.*

more conducting material present close to the plasma. However, the critical rotation velocity required to stabilize the continuous shell configuration completely is now $v_\phi^{crit} \approx 100$ km/s, higher by more than a factor of 2 than the required v_ϕ^{crit} for the actual segmented wall configuration of PBX-M. The corresponding mode frequency for the full wall is substantially lower than the mode frequency for the partial wall. This nicely illustrates the disadvantage of having too strong a coupling between the plasma and the wall: strong coupling inhibits the mode rotation, allowing resistive decay of wall eddy currents through the conducting plates. In order for the plates to behave as if they are perfectly conducting, and thereby stabilize the external kink, the wall eddy currents must be allowed to rotate with a frequency that is fast compared with the inverse *L/R* time of the plates. This is favoured by operating with $\hat{r}_w$ as close to $\hat{r}_c$ as possible.

Figure 13 shows the mode structure of the resistive wall eigenfunctions calculated using the actual PBX-M segmented shell geometry. Figure 13(a) shows the mode structure without plasma rotation and Fig. 13(b) shows the mode structure for $v_\phi \approx v_\phi^{crit}$, close to marginality. The mode structure with a resistive wall and $v_\phi = 0$ is virtually indistinguishable from the mode structure obtained by PEST using an ideal wall to partially stabilize the external kink. The $m = 1$ contribution is substantial owing to $q(0) < 1$, and the $m = 2, 3$ contributions peak towards the respective integral $q = 2, 3$ surface locations. For the case of substantial plasma rotation, however, the effects of sound wave damping are readily seen as resonances close to the rational q surfaces, particularly near $q = 1$ and $q = 2$.

6. SUMMARY AND CONCLUSIONS

The effect of a conducting shell on plasma performance has been studied in PBX-M. Comparing the performance of PBX-M with PBX, β/ϵ was increased by a factor of 1.4, owing to the addition of a conducting shell. For a series of plasma shapes (circular, D and bean) in PBX-M, chosen to have varying strengths of plasma–shell coupling, $n = 1$ external kink growth times were found to vary between the ideal plasma (Alfvén) time-scale and the *L/R* time-scale of the nearby conducting shell. Modes that grow on the *L/R* time-scale of the shell were observed to be quasi-stationary ($\omega/\Omega \ll 1$) in the laboratory frame, whereas modes that grow on the Alfvén time-scale were found to co-rotate with the plasma at approximately the plasma toroidal rotation velocity. Slight changes in the plasma conditions can cause dramatic changes in mode frequency, with rapid transition from quasi-stationary to rotating mode behaviour. These features are consistent with the theory of resistive wall modes of ideal plasmas.

Resistive wall mode theory has predicted the possibility of achieving complete stability of external kink modes if the plasma rotation velocity, v_ϕ, can be sustained beyond some v_ϕ^{crit} that depends on the plasma pressure and current profiles and the proximity of the

conducting wall to the plasma. The experimental 'edge' rotation velocity in PBX-M is 20 to 40 km/s while the NOVA-W analysis predicts $v_\phi^{crit} \approx 45$ km/s. The experimental plasma rotation velocity is therefore comparable to, but slightly lower than, the required v_ϕ^{crit} for complete stability. The connection bars between the upper and lower conducting plates in PBX-M are not included in the NOVA-W calculations. Their existence presumably places an additional constraint on the plasma perturbation and must consequently increase the plasma–shell coupling strength. As seen in Fig. 11, this additional coupling should increase the required v_ϕ^{crit}, making the experimental conditions of the reported experiments further from satisfying conditions for complete stability. A careful survey of experimental results with higher rotation velocities near the edge is highly desirable to assess further the viability of achieving complete stability of resistive wall modes with plasma rotation.

Ward and Bondeson [14] have presented numerical evidence that having multiple rational surfaces in the plasma at which sound wave damping can occur is advantagous for decreasing v_ϕ^{crit}. There are many such rational surfaces in the bean-shaped plasma configurations in PBX-M, and we note that $v_\phi^{crit} \approx 0.01 v_A$ is significantly lower than the calculated values for DIII-D and those projected for TPX. The damping at the $q = 1$ surface in PBX-M may be particularly effective, since the resonance is in a central region of high pressure. We may speculate that the 'reverse shear scenarios' proposed for TPX and ITER may be made more stable with respect to resistive wall external kinks by having $q(0)$ as high as possible, for example, $q(0) > 4.0$ and $2 < q_{min} < 3$, allowing efficient damping of sound waves at the central $q = 4$ and $q = 3$ surfaces.

In addition to the results pertaining to resistive wall modes, the PBX-M data have shown evidence for simultaneous excitation of two types of MHD instability. The two cases shown here were the observations of an $n = 1$, $\omega \approx 0$ growing mode along with an $n = 2$ rotating mode in a tightly coupled bean configuration and of an $n = 1$, $\omega \approx 0$ mode with an $n = 1$ fishbone in a loosely coupled circular plasma. These results indicate that MHD modes can coexist in the laboratory frame and in the plasma frame depending upon the instability energy source. It is not clear, at present, whether any interaction between the two modes takes place that can accelerate the thermal collapse process.

ACKNOWLEDGEMENTS

We are pleased to acknowledge useful discussions with R. Fitzpatrick, the contributions of the PBX-M Physics Group, and, in particular, the PBX-M operation staff, led by J. Semler.

REFERENCES

[1] NEVINS, W.M., et al., in Plasma Physics and Controlled Nuclear Fusion Research 1994 (Proc. 15th Int. Conf. Seville, 1994), Vol. 2, IAEA, Vienna (1995) 543.
[2] CONN, R.W., et al., in Plasma Physics and Controlled Nuclear Fusion Research 1990 (Proc. 13th Int. Conf. Washington, DC, 1990), Vol. 3, IAEA, Vienna (1991) 659.
[3] SEKI, Y., et al., ibid., p. 473.
[4] KIKUCHI, M., Nucl. Fusion **30** (1990) 265.
[5] THOMASSEN, K., et al., in Plasma Physics and Controlled Nuclear Fusion Research 1994 (Proc. 15th Int. Conf. Seville, 1994), Vol. 2, IAEA, Vienna (1994) 632.
[6] MANICKAM, J., et al., Phys. Plasmas **1** (1994) 1604.
[7] KESSEL, C., et al., Phys. Rev. Lett. **72** (1994) 1212.
[8] OZEKI, T., et al., in Plasma Physics and Controlled Nuclear Fusion Research 1992 (Proc. 14th Int. Conf. Würzburg, 1992), Vol. 2, IAEA, Vienna (1993) 187.
[9] FREDRICKSON, E.D., et al., Phys. Plasmas **2** (1995) 4216.
[10] STRAIT, E.J., et al., Phys. Rev. Lett. **74** (1995) 2483.
[11] JAHNS, G.L., et al., Nucl. Fusion **28** (1988) 881.
[12] KAYE, S.M., et al., Nucl. Fusion **28** (1988) 1963.
[13] BONDESON, A., WARD, D.J., Phys. Rev. Lett. **72** (1993) 2709.
[14] WARD, D.J., BONDESON, A., Phys. Plasmas **2** (1995) 1570.
[15] POMPHREY, N., et al., in Plasma Physics and Controlled Nuclear Fusion Research 1994 (Proc. 15th Int. Conf. Seville, 1994), Vol. 3, IAEA, Vienna (1996) 251.
[16] CHU, M.S., et al., Phys. Plasmas **2** (1995) 2236.
[17] BETTI, R., FREIDBERG, J.P., Phys. Rev. Lett. **74** (1995) 2949.
[18] FITZPATRICK, R., AYDEMIR, A.Y., Nucl. Fusion **36** (1996) 11.
[19] BOOZER, A.H., Phys. Plasmas **2** (1995) 4521.
[20] TURNBULL, A.D., et al., in Plasma Physics and Controlled Nuclear Fusion Research 1994 (Proc. 15th Int. Conf. Seville, 1994), Vol. 1, IAEA, Vienna (1994) 705.

[21] TAYLOR, T., et al., Phys. Plasmas **2** (1995) 2390.
[22] STRAIT, E.J., et al., in Controlled Fusion and Plasma Physics (Proc. 21st Eur. Conf. Montpellier, 1994), Vol. 18B, Part I, European Physical Society, Geneva (1994) 242.
[23] BELL, R., et al., Phys. Fluids B **2** (1990) 1271.
[24] OKABAYASHI, M., et al., in Controlled Fusion and Plasma Physics (Proc. 18th Eur. Conf. Berlin, 1991), Vol. 15C, Part I, European Physical Society, Geneva (1991) 133.
[25] OKABAYASHI, M., et al., in Plasma Physics and Controlled Nuclear Fusion Research 1986 (Proc. 14th Int. Conf. Kyoto, 1987), Vol. 1, IAEA, Vienna (1987) 275.
[26] BOL, K., et al., Phys. Rev. Lett. **57** (1986) 1981.
[27] HATCHER, R., OKABAYASHI, M., Integrated Shell Approach to Vertical Position Control on PBX-M, Rep. PPPL 3089, Princeton Plasma Phys. Lab., NJ (1995).
[28] HATCHER, R., et al., Am. Phys. Soc. Bull. **28** (1993) 2096.
[29] GRIMM, R.C., et al., J. Comput. Phys. **16** (1976) 253.
[30] CHANCE, M., et al., in Plasma Dynamics: Theory and Applications (Proc. 2nd Symp. Trieste, 1992), Univ. of Trieste, Trieste (1992) 15.
[31] ROBERTS, D.W., et al., Phys. Rev. Lett. **71** (1993) 1011.
[32] MANICKAM, J., et al., Phys. Rev. Lett. **21** (1983) 1959.

(Manuscript received 9 November 1995
Final manuscript accepted 7 February 1996)